nature materials

ARTICLES

PUBLISHED ONLINE: 6 NOVEMBER 2017 | DOI: 10.1038/NMAT5006

# Intracellular production of hydrogels and synthetic RNA granules by multivalent molecular interactions

Hideki Nakamura[1,2†], Albert A. Lee[1,2†‡], Ali Sobhi Afshar[3*], Shigeki Watanabe[1], Elmer Rho[2], Shiva Razavi[1,4], Allister Suarez[1,2], Yu-Chun Lin[1,2], Makoto Tanigawa[1,4], Brian Huang[2], Robert DeRose[1,2], Diana Bobb[1,2], William Hong[5], Sandra B. Gabelli[5,6,7], John Goutsias[3] and Takanari Inoue[1,2,4*]

**Some protein components of intracellular non-membrane-bound entities, such as RNA granules, are known to form hydrogels *in vitro*. The physico-chemical properties and functional role of these intracellular hydrogels are difficult to study, primarily due to technical challenges in probing these materials *in situ*. Here, we present iPOLYMER, a strategy for a rapid induction of protein-based hydrogels inside living cells that explores the chemically inducible dimerization paradigm. Biochemical and biophysical characterizations aided by computational modelling show that the polymer network formed in the cytosol resembles a physiological hydrogel-like entity that acts as a size-dependent molecular sieve. We functionalize these polymers with RNA-binding motifs that sequester polyadenine-containing nucleotides to synthetically mimic RNA granules. These results show that iPOLYMER can be used to synthetically reconstitute the nucleation of biologically functional entities, including RNA granules in intact cells.**

A hydrogel is a hydrophilic polymer network which can absorb water[1] with physico-chemical characteristics that can be tuned by changing relevant parameters. In a biological context, these highly variable properties enable hydrogel-like structures to serve versatile roles[2–4]. Recent works have found that biological hydrogel-like structures not only exist in extracellular space, but also inside cells[5–7]. Intracellular hydrogels serve vital functions, such as forming diffusion barriers or nucleating cellular activities[8–10]. Cytoskeletal filamentous networks, including actin and intermediate filaments such as neurofilaments, have also been implicated to form hydrogel-like structures[11,12].

Another significant intracellular structure that has been associated to hydrogels is the RNA granule. RNA granules are known to exhibit a phase separation-like behaviour and be subject to dynamic structural rearrangements that are often referred to as liquid droplet-like[6,9,13–20]. Many of their components contain low-complexity sequences, which actually form hydrogels when purified[6]. Although RNA granules are physiologically important[21–23], their structural organization and biological relevance remain uncharacterized. Development of synthetic hydrogels that behave similarly to RNA granules may become an alternative to understanding the relationship between their structure and function.

Synthetic hydrogels have long been studied in the field of biomedical engineering, primarily because their physical properties can be designed and manipulated to achieve a desired objective. However, past research has principally focused on extracellular applications[24,25], while little has been achieved inside cells. There are several studies describing intracellular delivery of hydrogels[26,27], but these studies have not been successful in directly demonstrating that intracellular hydrogels are biologically functional. This is primarily due to lack of an experimental paradigm that is capable of forming gels in an inducible manner with sufficiently fast kinetics to allow monitoring functionality before and after induction.

Another challenge in studying intracellular hydrogels is the absence of satisfactory methods for their evaluation. It is often not straightforward to claim the identity of an intracellular object as being a gel, owing to limited physical access. Reconstitution of the material *in vitro* is the most frequently adopted strategy[6,8,14,28], although the conditions *in vitro* may not necessarily recapitulate those in living cells. Therefore, a comprehensive understanding of the nature of induced hydrogels requires the development of a new paradigm.

In this study, we developed a novel approach that can induce hydrogel formation in living cells. We evaluated this approach *in silico*, *in vitro*, and *in cellulo*, supporting the identity of formed aggregates as hydrogels. Moreover, we functionalized these aggregates to selectively nucleate the molecular components of an RNA stress granule. These results demonstrate that our novel

[1]Department of Cell Biology, School of Medicine, Johns Hopkins University, Baltimore, Maryland 21205, USA. [2]Center for Cell Dynamics, Institute for Basic Biomedical Sciences, Johns Hopkins University, Baltimore, Maryland 21205, USA. [3]Center for Imaging Science, Whitaker Biomedical Engineering Institute, Johns Hopkins University, Baltimore, Maryland 21218, USA. [4]Department of Biomedical Engineering, Whitaker Biomedical Engineering Institute, Johns Hopkins University, Baltimore, Maryland 21218, USA. [5]Department of Biophysics and Biophysical Chemistry, School of Medicine, Johns Hopkins University, Baltimore, Maryland 21205, USA. [6]Department of Medicine, School of Medicine, Johns Hopkins University, Baltimore, Maryland 21287, USA. [7]Department of Oncology, School of Medicine, Johns Hopkins University, Baltimore, Maryland 21287, USA. †These authors contributed equally to this work. ‡Present address: Department of Molecular and Cell Biology, University of California Berkeley, Berkeley, California 94702, USA. *e-mail: afshar@jhu.edu; jctinoue@jhmi.edu

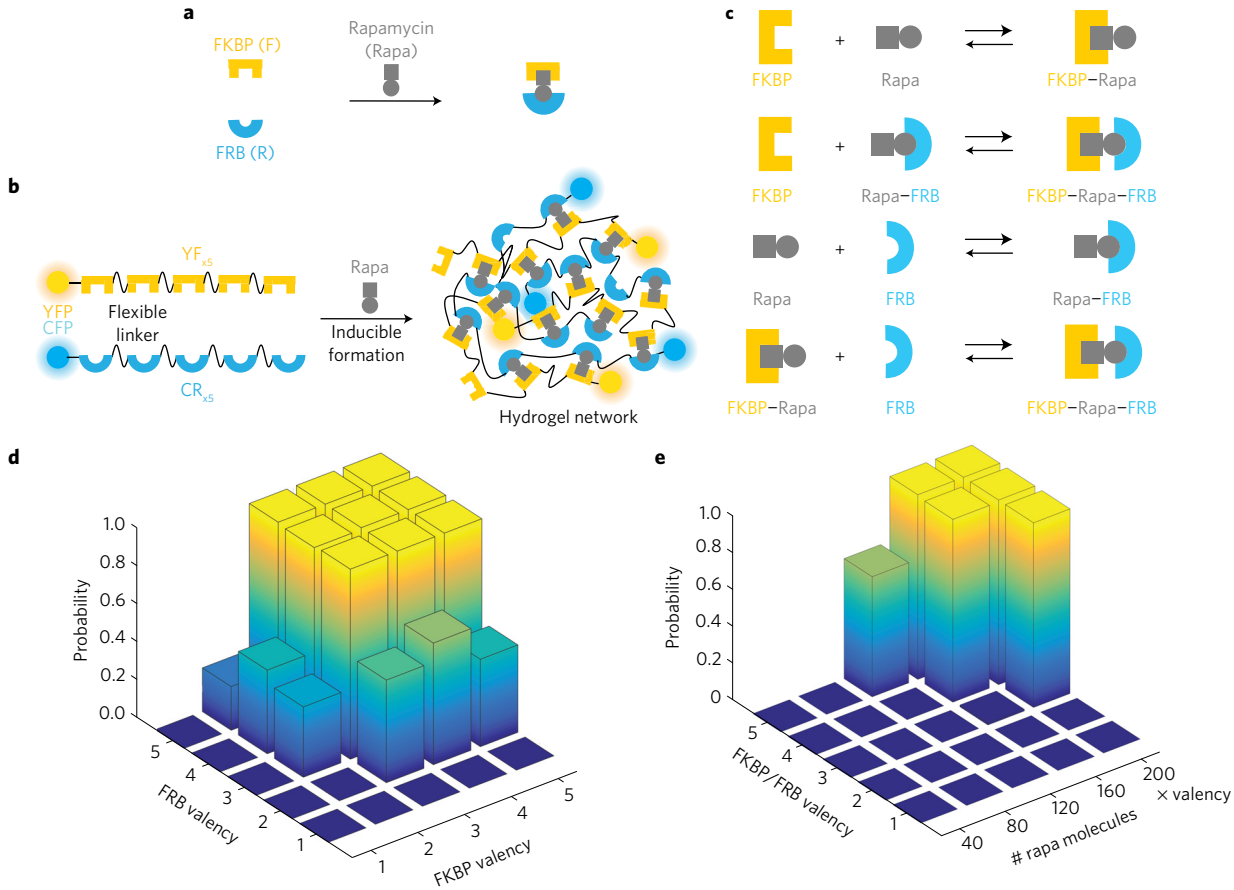


**Figure 1 | Schematic illustration of iPOLYMER and *in silico* analysis on network formation. a**, Rapamycin induces rapid, stable and specific binding between FKBP and FRB molecules. **b**, Two series of proteins, $YF_{xN}$ and $CR_{xM}$, were engineered to track their expression in cells: a yellow fluorescent protein (YFP) on up to five tandem repeats of an FKBP domain and a cyan fluorescent protein (CFP) on up to five tandem repeats on an FRB, spaced by 12 amino acid linker sequences. Mixing $YF_{x5}$ and $CR_{x5}$ (left) with rapamycin is expected to induce the formation of a hydrogel network (right). $YF_{xN}$ and $CR_{xM}$ contain *N* repeats of FKBP and *M* repeats of FRB with the same linkers, respectively. **c**, Four reversible reactions between monomeric FKBP, FRB and rapamycin molecules modelled in our simulations. Each binding unit in the tandem repeats of FKBP or FRB can undergo the four reactions in the presence of rapamycin. **d**, Estimated probabilities that iPOLYMER will produce aggregates of a threshold size of 100 or larger for different valence numbers of the FKBP and FRB molecules. An aggregate of size 100, as defined in Supplementary Information 1, comprises 25% of the total number of FKBP and FRB molecules initially present in the simulated system. The sharp increase in the probability values indicates that efficient polymerization can be achieved when the individual valence numbers of FKBP and FRB are at least three, with the total valence number of FKBP and FRB molecules being at least six. **e**, Estimated probabilities that iPOLYMER will produce aggregates of a threshold size of 100 or larger for different valence numbers of the FKBP and the FRB molecules and different numbers of rapamycin molecules, determined for each simulation by multiplying a base number of rapamycin molecules with the common valency of FKBP and FRB [for example, base rapa # (160) × valency (4) = rapa # (640)] to scale the effect of peptide valency on the number of binding sites against rapamycin. The observed sharp decrease in the probability values indicates that efficient polymerization requires a sufficient concentration of rapamycin. This implies that, in addition to the valence numbers of FKBP and FRB, the concentration of the dimerizing agent is expected to directly affect phase transition.

paradigm is a promising tool for elucidating possible roles of hydrogels in living cells, as well as for nucleating biological functions within cells.

## Design principles of the iPOLYMER strategy

To enable inducible hydrogel formation inside living cells, we introduced a novel strategy, iPOLYMER (intracellular production of ligand-yielded multivalent enhancers), that forms hydrogels composed of polymers held together via crosslinkers or direct interactions. We thus utilized a chemically inducible dimerization (CID) technique[29] to crosslink two polypeptide chains. In this system, the chemical agent rapamycin induces dimerization between two proteins, the FK506 binding protein (FKBP) and the FKBP–rapamycin binding protein (FRB), with high specificity and fast kinetics in living cells (Fig. 1a). We hypothesized that multiple copies of FKBP and FRB, interspaced with a linker, should undergo polymerization upon rapamycin addition, leading to a hydrogel-like network induced inside living cells (Fig. 1b).

## Computational modelling of polymer network formation

We first explored the feasibility of iPOLYMER *in silico* by modelling the underlying reactions and using kinetic Monte Carlo simulations (Fig. 1c, Methods and Supplementary Information 1). Using FKBP and FRB polypeptides with an equal number of binding sites, our simulations demonstrated, for valencies of three or more, a quick formation of relatively large aggregates, whereas only small aggregates were observed for valency two and none for valency one (Supplementary Movies 1–5).

We then computed the size distribution of the molecular aggregates at distinct time points (Supplementary Information 1 and Supplementary Figs 1.3–1.7). At valencies of three or more, the size distribution gradually spreads over larger sizes, whereas more

aggregates with larger sizes are formed as the valency increases. This observed strong dependency on valency was consistent with previous findings[30,31].

We further demonstrated that, at valence number three or more, the size distribution is initially unimodal but eventually becomes bimodal, indicating the coexistence of two distinct phases (Supplementary Information 1 and Supplementary Figs 1.5–1.7). Further evidence of phase transition was demonstrated by estimating the probabilities of iPOLYMER to produce large aggregates for different valencies (Fig. 1d) and different rapamycin concentrations (Fig. 1e).

To evaluate the size-dependent sieving property of an aggregate, we constructed and implemented a graph representation of the aggregate, which models the aggregate as a sieve, and defined its effective pore size (EPS) (Supplementary Information 1). This allowed us to computationally predict a range of plausible EPS values (10–28 nm) for aggregates formed by iPOLYMER.

## iPOLYMER aggregate formation in living cells

We then performed iPOLYMER experiments in living cells. We generated two series of polypeptides (Fig. 1b): a yellow fluorescent protein (YFP), on up to five tandem repeats of an FKBP ($YF_{xN}$, $N = 1, 2, 3, 4, 5$), and a cyan fluorescent protein (CFP) on tandem repeats of an FRB ($CR_{xM}$, $M = 1, 2, 3, 4, 5$). We co-expressed the highest-valence number pair ($YF_{x5}$, $CR_{x5}$) in COS-7 cells and added rapamycin. Cells with high expression of both polypeptides initially exhibited diffuse fluorescence signals that rapidly turned into puncta upon rapamycin addition (Fig. 2a and Supplementary Movie 6). These puncta steadily grew in size during prolonged rapamycin treatment up to 24 h (Supplementary Figs 5.1 and 5.2). The experiment was carried out with a Förster resonance energy transfer (FRET) measurement between CFP and YFP, and increasing FRET values were observed in the cytosol within 5 min of rapamycin addition, whereas a continuous FRET increase was observed at the puncta that emerged at later time points (Fig. 2a and Supplementary Fig. 5.3 and Supplementary Movie 6). The puncta formation was not observed in dimethylsulfoxide (DMSO)-treated cells (Fig. 2b). FRET ratio fold-change was significantly greater at the puncta compared to that in the cytosol (Fig. 2c). We found that two puncta occasionally coalesced into a larger one with minimal morphological reorganization (Supplementary Fig. 5.1), reflecting the practically irreversible nature of rapamycin-induced CID in cells[32]. We also performed fluorescent recovery after photobleach (FRAP) analysis of the fluorescent polypeptides at or within the puncta to reveal little remodelling (Supplementary Information 2).

We noticed that the series of polypeptides, $YF_{xN}$, and $CR_{xM}$, tended to accumulate in the nucleus rather than in the cytosol, leading to puncta formation in the nucleus (Supplementary Information 3). To overcome the nuclear accumulation, we hereafter used polypeptides fused with N-terminal nuclear export signal, termed $cytoYF_{xN}$ and $cytoCR_{xM}$, unless specified. Details regarding the subcellular targeting of the polypeptides are provided in Supplementary Information 3.

## Valence dependency of iPOLYMER puncta formation

To experimentally explore the effect of valency on puncta formation, we carried out FRET measurement in cells co-transfected by the constructs ($YF_{xN}$, $CR_{xN}$), $N = 1, 2, 3, 4$, and observed noticeable differences in the FRET kinetics (Supplementary Fig. 5.3). We further explored the effect of valency on the probability of puncta formation by testing all 25 different pairs ($cytoYF_{xN}$, $cytoCR_{xM}$), for $N, M = 1, 2, 3, 4, 5$. When $N + M \leq 5$, less than 15% of cells formed puncta (Fig. 2d,e), whereas the percentage dramatically increased at large $N + M$, showing resemblance to the results *in silico* (Fig. 1d).

## Molecules but not vesicles pass through iPOLYMER puncta

One essential feature of hydrogels is their molecular sieving property[28]. To test if the iPOLYMER-induced puncta retain this property, we performed FRAP at the puncta against fluorescently labelled diffusion probes independent of iPOLYMER polypeptides. First, the red fluorescent protein mCherry was co-transfected in cells with $cytoYF_{x5}$ and $cytoCR_{x5}$. Following rapamycin addition, mCherry was photobleached at a single spot within the puncta (Fig. 3a,b and Supplementary Fig. 5.4a) and the fluorescence recovery kinetics were analysed (see Methods, Supplementary Fig. 5.4b,c). The kinetics of the recovery at the puncta were similar to those outside the puncta (Fig. 3b–d and Supplementary Fig. 5.5a). We then repeated the experiment using a larger diffusion probe, mCherry fused to β-galactosidase, which forms a tetramer complex with a diameter of roughly 16 nm (ref. 33). The FRAP kinetics of mCherry-β-galactosidase were also similar to those outside the puncta (Fig. 3b and Supplementary Fig. 5.5b). Since the probe diameter is greater than that of most soluble solitary proteins[33], we reasoned that proteins generally pass through the puncta without significant filtering. To test if larger entities can pass through the puncta, we examined the movement of trans-Golgi vesicles, visualized with mCherry-TGN38 expression. Accordingly, we found that movement of mCherry-labelled vesicles was significantly slowed down upon hitting the puncta ($24 \pm 0.090\ nm\ s^{-1}$ before hitting the puncta and $5.8 \pm 0.011\ nm\ s^{-1}$ after; Fig. 3e), while the vesicles had never penetrated through the puncta. Taken together, these intracellular evaluations implied that iPOLYMER-generated puncta in living cells retain a molecular sieving property, allowing most soluble proteins to pass through but preventing penetration of larger entities, such as vesicles. We estimated the EPS to be in the range of 16–70 nm, since the TGN38-labelled vesicles are reported to have a diameter of around 70–140 nm (ref. 34).

## Ultrastructural analysis of iPOLYMER puncta

Subsequently, we compared the morphology of iPOLYMER puncta to that of a cytosolic protein-based structure which has been related to a hydrogel. A stress granule is a protein-RNA assembly that is thought to undergo sol-gel-like phase transition upon various stress conditions[35], and its ultrastructure has been reported by electron microscopy (EM)[36]. We used correlative EM to compare the morphology of iPOLYMER puncta with that of stress granules (see Methods). Electron-dense, fibrillo-granular structures were observed at the iPOLYMER puncta (Fig. 3f), with these structures lacking apparent membrane and morphologically resembling the actual stress granules (Fig. 3f).

## *In vitro* characterization of aggregates as hydrogels

To further explore the properties of hydrogel-like iPOLYMER puncta, we purified $YF_{x5}$ and $CR_{x5}$ to reconstitute rapamycin-induced hydrogels *in vitro*. When $YF_{x5}$ and $CR_{x5}$ were mixed at $>5\ \mu M$, small puncta with fluorescence and elevated FRET efficiency were observed after adding $1\ \mu M$ rapamycin (Supplementary Fig. 5.6). When the concentrations were increased to $100\ \mu M$ for both peptides and $500\ \mu M$ for rapamycin, the solution became instantaneously turbid upon mixing (Fig. 4a), containing dense and irregularly shaped puncta (Fig. 4b). These puncta were not observed when DMSO was added, or in the experiment without $CR_{x5}$ (Fig. 4c). Confocal imaging revealed the interior structure of the puncta to be irregular and heterogeneous (Supplementary Fig. 5.7). We then spun down the puncta to obtain a coloured pellet that was structurally stable and optically translucent, with an elastic response to deformation (Fig. 4d and Supplementary Movie 7). Removal of the ambient solution did not result in an immediate loss of the pellet's shape or colour (Fig. 4d), suggesting an ability to absorb and retain water. Weighing the material before and after drying confirmed the water content to be at least 75.2% (Supplementary Fig. 5.8). We

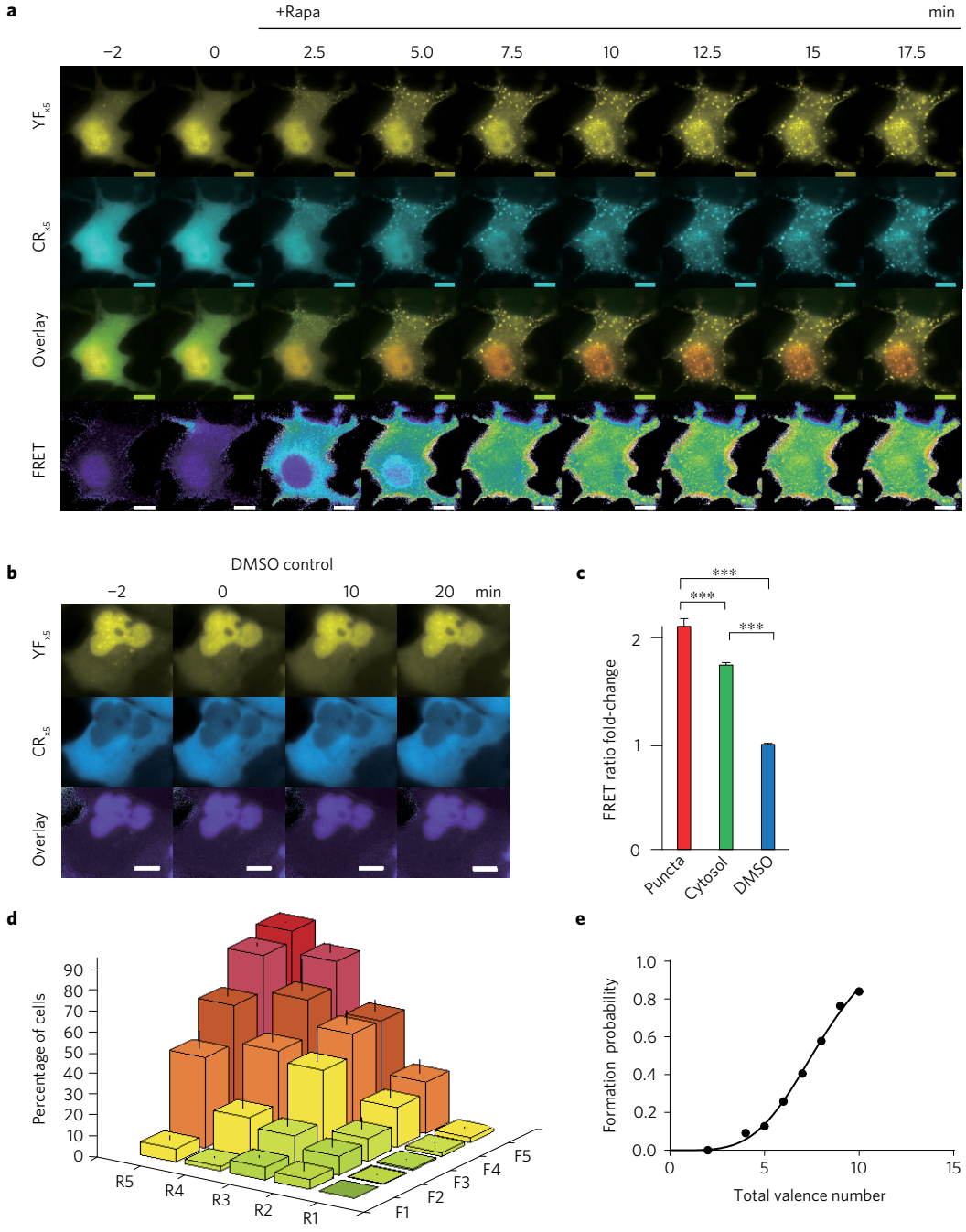


**Figure 2 | iPOLYMER puncta formation in living cells. a**, Time-lapse imaging of fluorescent puncta formation in COS-7 cells at indicated times relative to the addition of rapamycin. Scale bars, 10 μm. Punctate structures enriched with CFP, YFP, and FRET signals start to emerge within 5 min after 333 nM rapamycin addition. **b**, Time-lapse imaging of DMSO-treated cells. Scale bars, 10 μm. No formation of fluorescent puncta was observed. **c**, The FRET ratio fold-change at the puncta (puncta) and that in the cytosol without puncta (cytosol) in rapamycin-treated cells are shown together with the fold-change in DMSO-treated cell cytosol (DMSO). The FRET ratio change was significantly greater at puncta compared to that in the cytosol, which still was significantly greater than in DMSO-treated cells. Error bars: s.e.m. ***, $p < 0.01$. **d**, Frequency of iPOLYMER puncta formation plotted against valence numbers in FKBP and FRB constructs. $F_N$ represents valence number of cytoYF$_{xN}$, whereas $R_M$ represents cytoCR$_{xM}$. **e**, Probability of iPOLYMER formation plotted against the total valance number $N+M$. To avoid bias, the combinations ($N=1$, $M>1$) and ($N>1$, $M=1$) were excluded from the data. Note that peptides with single valency should not lead to network formation, confirmed by the rare puncta formation in **b** for F1 or R1.

therefore concluded that the rapamycin-induced aggregates of the pair (YF$_{x5}$, CR$_{x5}$) were indeed hydrogels.

## iPOLYMER hydrogel as an *in vitro* molecular sieve

To assess the molecular sieving potential of the hydrogel *in vitro*, we performed diffusion assays using fluorescent diffusion tracers of varying sizes (4.3, 6, and 20 nm in diameter, see Methods). We infused these tracers into a solution containing spun-down rapamycin-induced hydrogel, and measured the ratio of fluorescence intensity inside and outside the hydrogel under a confocal microscope (Fig. 4e,f). Whereas the 4.3-nm tracer penetrated into the hydrogel almost freely, the 6-nm and 20-nm tracers were clearly excluded (Fig. 4e,f and Supplementary Fig. 5.9). We thus estimated the EPS of the hydrogel *in vitro* to be 4.3–6 nm.

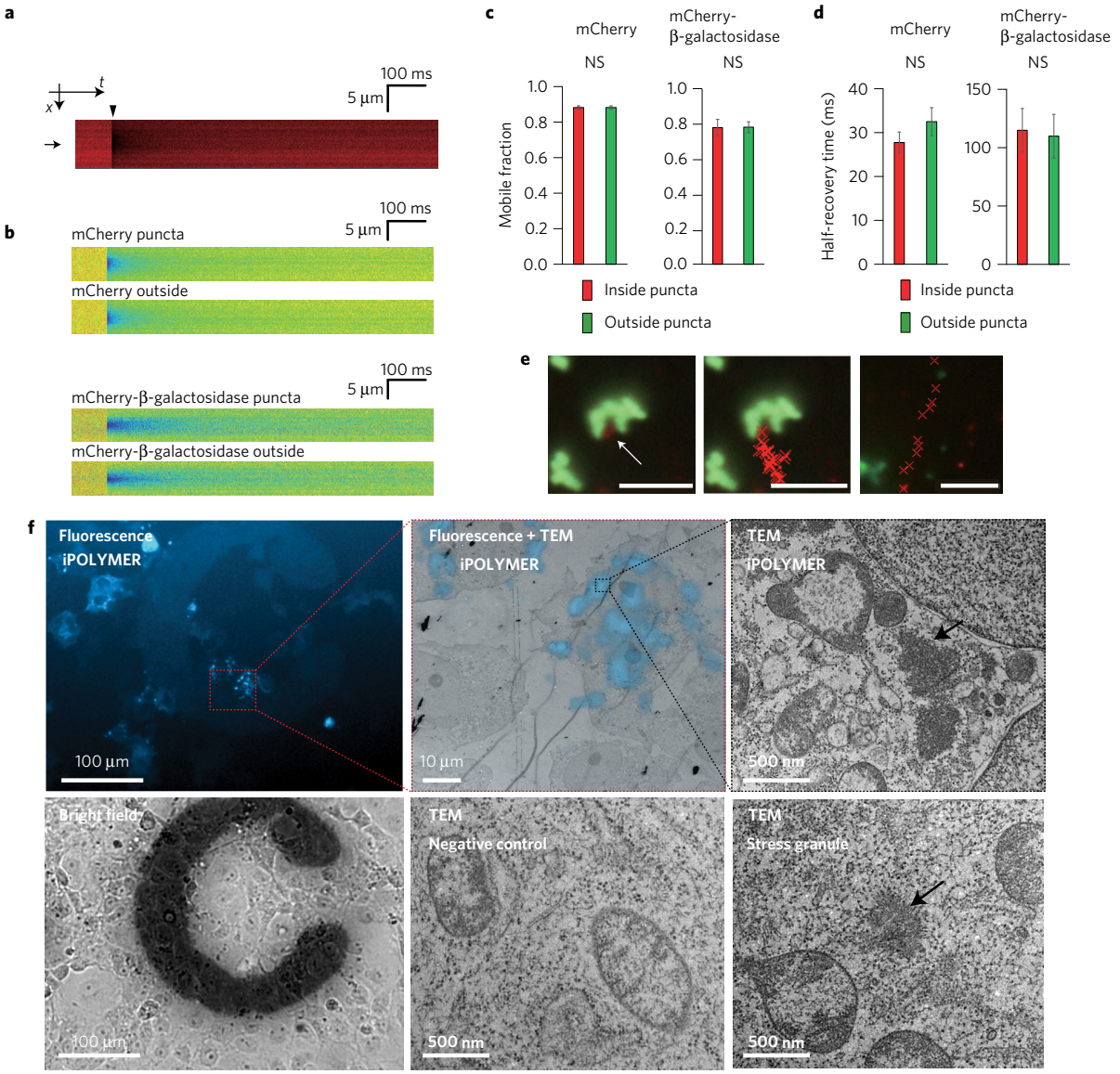


**Figure 3 | Biophysical and ultrastructural analysis of iPOLYMER in living cells. a**, Fluorescence intensity profile of mCherry in the cytosol in a line-scan FRAP experiment is shown in an *x*–*t* presentation. The fluorescence was photobleached at a single spot located in the middle of the puncta, as indicated by an arrow. The arrowhead indicates the time of bleaching. **b**, Representative normalized fluorescent intensity profiles shown for each experimental condition as a pseudo-coloured image. Fluorescence recovery kinetics quantified from the data for mCherry and mCherry-β-galactosidase signals inside (puncta) or outside (outside) the puncta. **c**, Mobile fraction of the fluorescence recovery at the puncta (inside puncta) or in the cytosol without any puncta (outside puncta) are shown for mCherry and mCherry-β-galactosidase. No significant difference was observed. *p*-value > 0.05, error bars: s.e.m. **d**, Half-recovery time of the fluorescence recovery at the puncta (inside puncta) or in the cytosol without any puncta (outside puncta) are shown for mCherry and mCherry-β-galactosidase. No significant difference was observed. *p*-value > 0.05, error bars: s.e.m. **e**, Representative images of a mCherry-TGN38-labelled vesicle in contact with iPOLYMER punctum, indicated by the white arrow (left panel). The red crosses in the middle and right panels mark the position of the vesicle during a period of 150 s at 5 s intervals when colliding with the punctum (middle panel) and in the cytosolic region free of visible puncta (right panel). Scale bars, 5 µm. **f**, Transmitted EM (TEM) images of iPOLYMER puncta were obtained in COS-7 cells by correlating the CFP–$FRB_{x5}$ fluorescence image (top-left panel (fluorescence)) with the TEM image (top-middle panel, shown as overlaid with correlated fluorescence image (fluorescence + TEM iPOLYMER); scale bar, 10 µm). The cells with apparent iPOLYMER puncta induced by 333 nM rapamycin administration were identified before EM imaging by referring to the grid pattern in the bright-field image (bottom-left panel (bright field); scale bar, 100 µm). A high-magnification image of an iPOLYMER punctum is shown in the top-right panel (TEM iPOLYMER; scale bar, 500 nm), compared to the TEM image of an actual stress granule induced by 30 min incubation with 0.5 mM arsenite (bottom-right panel (TEM stress granule); scale bar, 500 nm). A negative control EM image of the cytosol without stress granule induction is also shown in the bottom-middle panel (TEM negative control; scale bar, 500 nm). The iPOLYMER punctum exhibited an electron-dense granulo-fibrillar structure (black arrow in the TEM iPOLYMER) without any membranes surrounding it, resembling the actual stress granule (black arrows in TEM stress granule).

## Functionalizing iPOLYMER gels

We next aimed to utilize iPOLYMER hydrogels as a scaffold to rapidly nucleate a biological entity. We expected that iPOLYMER can be used to study RNA granules, due to their relation to gels and their morphological resemblance to iPOLYMER puncta *in situ* (Fig. 3f). Previous studies have shown that one stress granule component, TIA-1, self-assembles upon treatment with arsenite, turning into a stress granule[37,38]. TIA-1 consists of two domains:

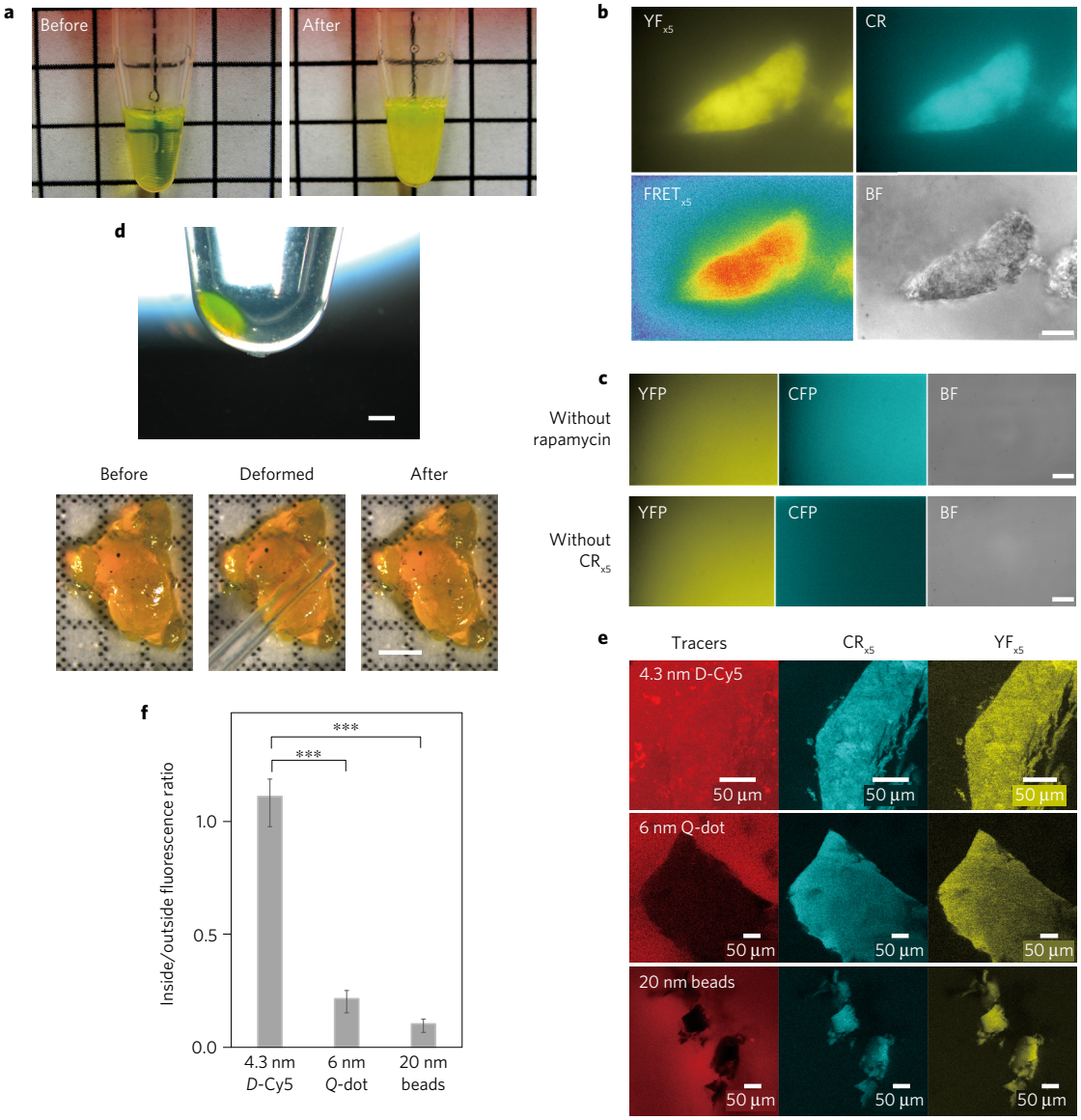


**Figure 4 | *In vitro* characterization of iPOLYMER. a**, Mixing 100 μM $YF_{x5}$ and 100 μM $CR_{x5}$ (left) with 500 μM rapamycin in a 1.5 ml tube instantly led to a turbid appearance (right). Size of grid: 0.5 cm. **b**, Fluorescent, FRET, and bright-field (BF) microscopic images of iPOLYMER aggregates formed *in vitro*. Scale bar, 20 μm. **c**, Mixing 100 μM $YF_{x5}$ with 100 μM $CR_{x5}$ and DMSO did not form any aggregates (without rapamycin), and the same was true when mixing 100 μM $YF_{x5}$ with 500 μM rapamycin (without $CR_{x5}$). **d**, Aggregates were collected by centrifuge and observed under a dissection microscope. Coloured pellet was observed after centrifugation and removal of the supernatant (top panel). The pellet was isolated on a coverslip for further observation and experimentation (lower panel). The fragments were translucent with clearly defined shapes (before), and the aggregates retained their three-dimensional shape and translucent appearance after the removal, demonstrating the identity as a hydrogel. The hydrogel was mechanically deformed with a micropipette tip (deformed), and was confirmed to regain its original shape (after), which was almost indistinguishable from that before applying the deformation (before). Scale bars, 1 mm. **e**, Pore-size evaluation of the iPOLYMER hydrogel *in vitro*. Hydrogels collected by centrifuge were re-suspended with fluorescent tracers with distinct diameters, and observed under a confocal fluorescence microscope. Whereas a D-Cy5 tracer with 4.3-nm-diameter penetrated into the hydrogel (top panel), 6-nm-diameter Q-dot (middle panel) and 20-nm-diameter fluorescent beads (lower panel) were clearly excluded from the hydrogel. **f**, The ratio of the tracer fluorescence intensity inside the hydrogel to that of outside the gel for each tracer molecule. Error bars, s.e.m. ***, $p < 0.01$. The observed difference of the ratios associated with D-Cy5 (4.3 nm) and Q-dot (6 nm) suggest that the hydrogel functions as a molecular sieve with an effective pore size of 4.3–6 nm.

an RNA recognition motif (RRM) that binds to polyadenine (Poly-A) containing RNAs, and a prion-related domain (PRD), which self-assembles into a gel-like state. It was found that when the RRM domain is fused with an exogenous aggregation-promoting domain in place of PRD, RNA granules would form spontaneously[37]. To reproduce the formation of RNA granules in an inducible manner, we replaced the PRD domain with the iPOLYMER component $CR_{x5}$, and produced a functionalized protein RRM-$CR_{x5}$. We then induced the formation of intracellular hydrogels with co-expressed cytoYF$_{x5}$ (Fig. 5a). After administering rapamycin for 1 h, cells were immunostained for PABP-1, an RNA-binding protein known to accumulate in stress granules. The functionalized iPOLYMER puncta were colocalized with PABP-1 (Fig. 5b). This suggested that the functionalized iPOLYMER puncta, or the stress granule analogues, could sequester poly-A containing mRNAs in a similar fashion as the actual stress granules. PABP-1 was not accumulated in iPOLYMER puncta without functionalization (Supplementary Fig. 5.10). We further evaluated the

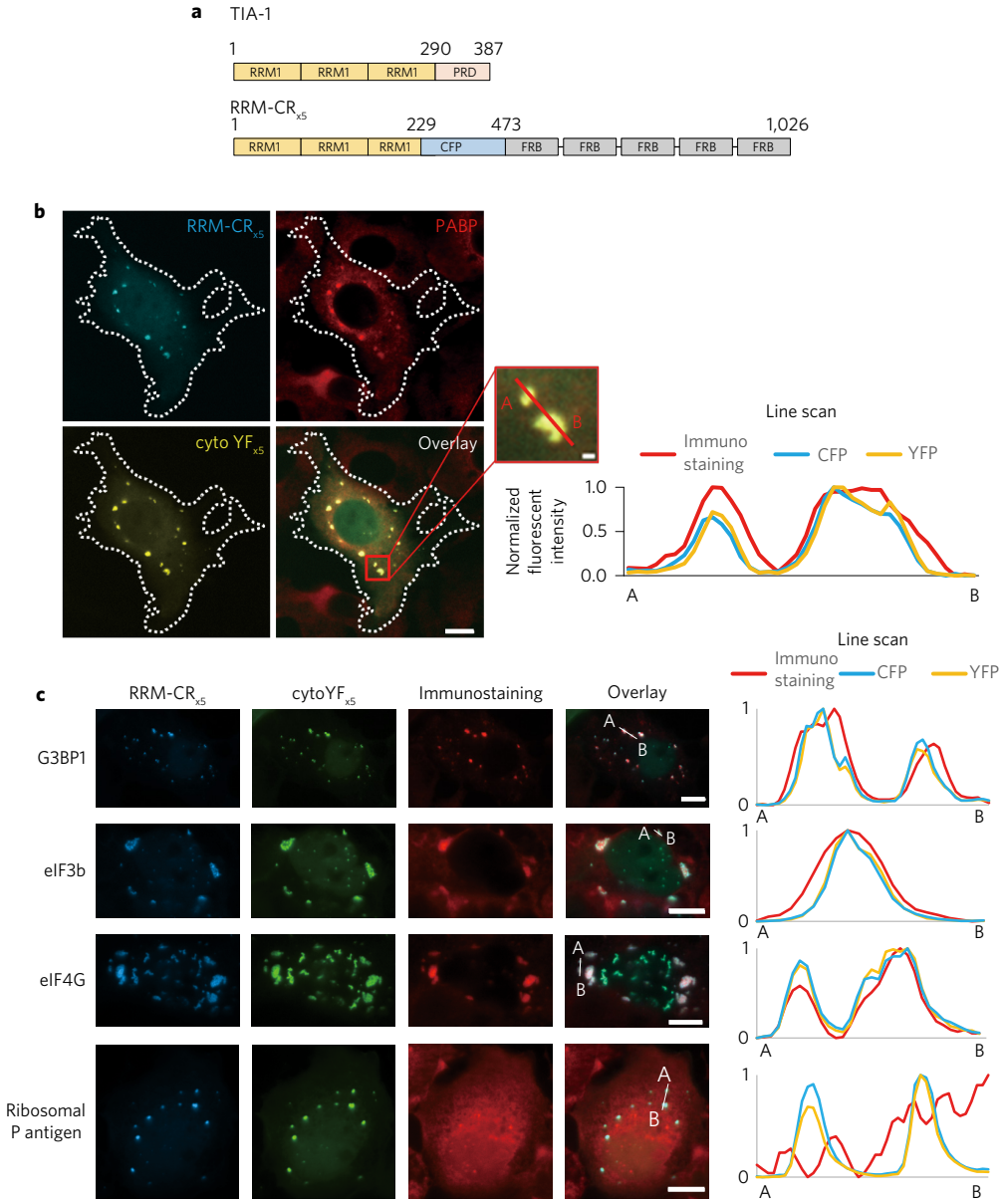


**Figure 5 | Reconstituting RNA granules by using iPOLYMER as scaffold. a**, Schematic illustration of the RRM-$CR_{x5}$ construct used in RNA granule reconstitution. Three RRM domains from TIA-1 were fused to $CR_{x5}$. **b**, Immunostaining images of COS-7 cells expressing RRM-$CR_{x5}$ and cytoY$F_{x5}$ treated with rapamycin to form iPOLYMER puncta. Scale bar, 10 μm. The line-scan plot from A to B in the enlarged image confirms colocalization of endogenous PABP with the functionalized iPOLYMER puncta. **c**, Immunostaining of the RRM-functionalized iPOLYMER with the universal stress granule markers G3BP1, eIF3b, and eIF4G and corresponding line-scan plots from A to B shown in each overlay image. As a negative control, ribosomal P antigen, which does not accumulate in the stress granules, was also stained. RRM-functionalized synthetic analogue of RNA granules accumulated all the three stress granule markers (7/17 cells showed accumulation of G3BP1, 12/29 cells of eIF3b, and 8/15 cells of eIF4G), while ribosomal P antigen accumulation was not observed (0/27 cells).

requirement for the RNA sequestration by targeting functionalized iPOLYMER puncta onto the surface of lysosomes, and concluded that the cytosolic environment is required for mRNA accumulation (Supplementary Information 4).

## iPOLYMER-based stress granule analogues

To further characterize the iPOLYMER-based stress granule analogues, generated as described earlier, we performed immunostaining against G3BP1, eIF3b, and eIF4G, three mRNA-associated proteins that are universally present in stress granules[39]. In addition to these, we included a ribosomal large subunit P antigen, a protein that also binds to mRNAs and regulates translation. Unlike the previous three RNA-binding proteins, the ribosomal P antigen does not accumulate in stress granules, and this is thought to be responsible for a critical function of stress granules—that is, a halted translation of homeostatic proteins[39,40] (Supplementary Fig. 5.11). Subsequent immunostaining against the four proteins revealed colocalization of the three stress granule markers, but not of ribosomal P antigen, with the stress granule analogues (Fig. 5c). The accumulation was dependent on the presence of both rapamycin and RRM (Supplementary Fig. 5.10).

## Development of light-inducible, reversible iPOLYMER-LI

The stress granule analogues still differ from their physiological counterpart in several key properties, with irreversibility in granule formation being one of the most striking differences. Irreversible

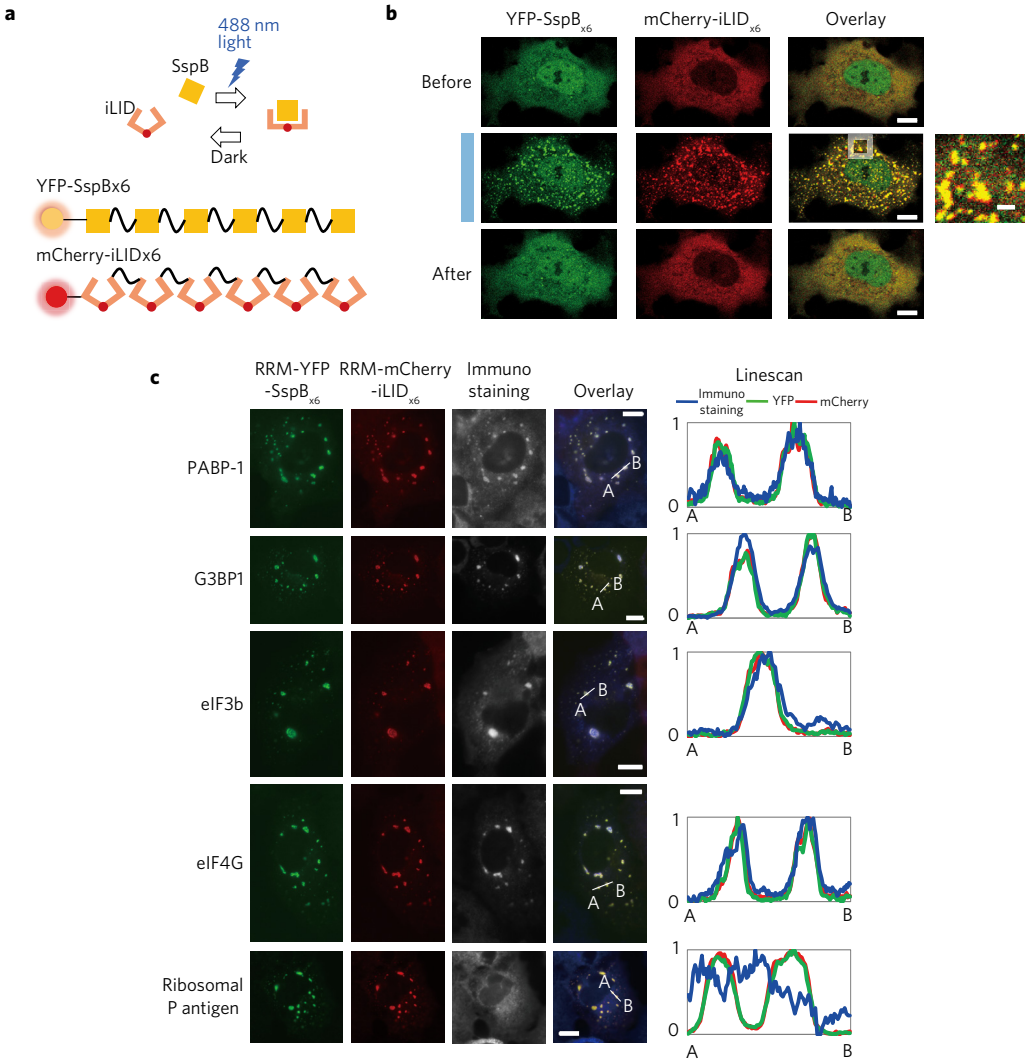


**Figure 6 | Light-inducible and reversible iPOLYMER-LI succeeded in RNA granule reconstitution. a**, Designs of light-inducible iPOLYMER-LI constructs. The two peptides, SspB and iLID, bind to each other upon blue light (488 nm) stimulation in a reversible manner (top panel). YFP-SspB$_{x6}$ and mCherry-iLID$_{x6}$ contain six repeats of iLID and SspB, respectively, spaced by nine amino acid linker sequences (lower panel). Due to the design principle similar to YF$_{x5}$ and CR$_{x5}$, the two peptide chains are expected to form a polymer network upon light irradiation. However, unlike YF$_{x5}$ and CR$_{x5}$, the network formation is reversible. **b**, Reversible puncta formation by YFP-SspB$_{x6}$ and mCherry-iLID$_{x6}$. The cell was irradiated with a 488 nm laser before each frame during the stimulus. The blue rectangle labels images observed under stimulus. Light-induced formation of the protein aggregates was readily observed within 15 min (middle panel and magnified detail). By ceasing stimulation, the aggregates were dispersed within 7.5 min (After), demonstrating the reversible nature of the light-inducible version of iPOLYMER, iPOLYMER-LI. Scale bars, 10 μm; 2 μm for magnified image. **c**, Immunostaining of the RRM-functionalized iPOLYMER-LI with the universal stress granule markers PABP-1, G3BP1, eIF3b, and eIF4G and corresponding line-scan plots from A to B shown in each overlay image. Immunostaining results are shown in blue in overlay images. As a negative control, ribosomal P antigen, which does not accumulate in the stress granules, was also stained. RRM-functionalized iPOLYMER-LI puncta (YFP-SspB$_{x6}$ and mCherry-iLID$_{x6}$) accumulated all the three stress granule markers (33/65 cells showed accumulation of PABP-1, 25/40 cells of G3BP1, 23/51 cells of eIF3b, and 52/75 cells of eIF4G), while ribosomal P antigen accumulation was not observed (0/75 cells). Scale bars, 10 μm.

remodelling within the rapamycin-based iPOLYMER puncta could limit the application of the technique. To overcome this issue, we applied the same design principle (that is, using multivalent dimerizer polypeptides) to light-inducible dimerizers, which are reversible. More specifically, we used iLID (improved light-inducible dimer) and its binding partner, SspB, which dimerize upon irradiation with blue light[41]. We synthesized six tandem iLIDs and six tandem SspBs, which were fused to YFP and mCherry, respectively (Fig. 6a). When co-expressed in cells, these two multivalent polypeptides formed cytosolic aggregates upon laser illumination at 488 nm in a reversible manner (Fig. 6b). The aggregates could also be induced subcellularly and repetitively (Supplementary Fig. 5.12 and Supplementary Movie 8). We termed this reversible iPOLYMER as iPOLYMER-LI (intracellular production of light-yielded multivalent enhancers with light inducibility).

## iPOLYMER-LI produced stress granule analogues

We then evaluated iPOLYMER-LI in the context of stress granule analogues. We fused RRM domains to both iPOLYMER polypeptides, produced puncta by RRM-mCherry-iLIDx6 and RRM-YFP-SspBx6, and performed immunostaining analysis. As a result, we confirmed accumulation of all four stress granule markers, PABP-1, G3BP1, eIF3b, and eIF4G, at the functionalized iPOLYMER-LI puncta, while we did not observe any accumulation of ribosomal P antigens (Fig. 6c). The accumulation was light-stimulus-dependent and RRM domain-dependent (Supplementary Fig. 5.13).

**Table 1 | Comparison between iPOLYMER- and iPOLYMER-LI-based stress granule analogues and the actual stress granules.**

| | | Accumulation of RNA-associated proteins | | | | | Reversibility |
|---|---|---|---|---|---|---|---|
| | | Universal SG markers | | | | Non-Marker | |
| | | PABP-1 | G3BP1 | eIF3b | eIF4G | Ribosomal P antigen | |
| Stress Granules (SGs) | | ✓ | ✓ | ✓ | ✓ | × | Reversible |
| 'Synthetic' SG analogues | TIA-1 RRM-iPOLYMER (rapamycin) | ✓ | ✓ | ✓ | ✓ | × | Irreversible |
| | TIA-1 RRM-iPOLYMER-LI (light) | ✓ | ✓ | ✓ | ✓ | × | Reversible |

Stress granule analogues are similar to their physiological counterparts in the specific recruitment of universal stress granule markers. Rapamycin-induced analogues differ from physiological stress granules in reversibility of the formation process, while iPOLYMER-LI-based analogues have overcome the discrepancy.

These results revealed that iPOLYMER-LI produced stress granule analogues not only in terms of selective molecular components, but also of reversible mechanisms of puncta formation (Table 1).

## Concluding remarks

To overcome difficulties in forming hydrogels *in situ*, we first developed a realistic computational model of iPOLYMER. Simulation results using this model rationally guided our experimental design and provided further validation of our experimental findings and conclusions in our *in vitro* reconstitution of the polypeptide network. More specifically, our computational model exhibited valency-dependent polymer network formation with striking resemblance to our experimental results, in terms of its dependency on valency and EPS (for detailed comparison, see Supplementary Information 1). We also experimentally estimated the EPS of the hydrogels *in vitro* to be 4.3–6 nm. These sizes, however, were significantly smaller than the ones estimated in living cells (16–70 nm), a discrepancy that could be explained by differences in protein and rapamycin concentrations used in our experiments. Moreover, our experimental procedure required centrifugation of the hydrogels during the *in vitro* evaluation, which may have affected the pore size as well.

Here, we took advantage of the iPOLYMER paradigm to induce the formation of stress granule analogues in living cells. Although there are several suggestions in the literature that stress granules resemble hydrogels, it has recently been claimed that many non-membrane-bound organelles, including RNA granules such as stress granules, have a common dynamic feature, being often referred to as liquid droplet-like[9,13]. Indeed, one report indicates that a given low-complexity domain can form hydrogels *in vitro*, whereas it shows liquid droplet-like behaviour *in situ*, and demonstrates that the molecular conformation is similar in both cases[18]. However, it is still unknown how these distinct physical properties (static hydrogels versus dynamic liquid droplets) emerge. We believe that our iPOLYMER strategy will in the future contribute to understanding the structure and function of RNA granules. Notably, design principles of iPOLYMER could dictate its functionality. For instance, rapamycin-based iPOLYMER granules exhibited constant growth in size due to iPOLYMER's irreversible nature, which may allow these granules to go beyond optimal length scale to be functional as an RNA granule. In this case, optogenetic iPOLYMER-LI may be favoured due to its reversible and precise operation in space and time. In addition, we cannot fully exclude the possibility that iPOLYMER/iPOLYMER-LI puncta formation itself becomes a stress to cells, activating stress pathways that may secondarily affect molecular features of iPOLYMER-induced RNA granule analogues.

Another possible application of iPOLYMER would be to reconstitute a nuclear pore complex (NPC), which utilizes a FG-repeat-based reversible hydrogel for its selective permeability of molecules[28]. Synthetically reconstituting an NPC-like permeability barrier may result in an interesting insight into the NPC biology.

From a technical point of view, iPOLYMER has several advantages over previous counterparts that can form protein-based aggregates in living cells[42–46]. Besides opening a possibility for the determination of the detailed physical nature of these aggregates, puncta formation using iPOLYMER does not rely on protein unfolding or domains from pathogenic proteins, both of which can possibly trigger intrinsic cellular responses, unlike several recently reported techniques[44,46]. Finally, iPOLYMER provides a flexible and generalizable framework, as indicated by the development of the optogenetic iPOLYMER-LI. Taken together, iPOLYMER, armed with spatio-temporal control, could become a powerful means for studying granular structures in cells and gel-like aggregates exhibiting neurodegenerative toxicity[47].

## Methods

Methods, including statements of data availability and any associated accession codes and references, are available in the online version of this paper.

Received 31 December 2015; accepted 8 September 2017; published online 6 November 2017

## References


1. Hoffman, A. S. Hydrogels for biomedical applications. *Adv. Drug Deliv. Rev.* **54,** 3–12 (2002).
2. Frantz, C., Stewart, K. M. & Weaver, V. M. The extracellular matrix at a glance. *J. Cell Sci.* **123,** 4195–4200 (2010).
3. Lieleg, O. & Ribbeck, K. Biological hydrogels as selective diffusion barriers. *Trends Cell Biol.* **21,** 543–551 (2011).
4. Lai, S. K., Wang, Y.-Y., Wirtz, D. & Hanes, J. Micro- and macrorheology of mucus. *Adv. Drug Deliv. Rev.* **61,** 86–100 (2009).
5. Weber, S. C. & Brangwynne, C. P. Getting RNA and protein in phase. *Cell* **149,** 1188–1191 (2012).
6. Kato, M. *et al*. Cell-free formation of RNA granules: low complexity sequence domains form dynamic fibers within hydrogels. *Cell* **149,** 753–767 (2012).
7. Hyman, A. A. & Simons, K. Cell biology. Beyond oil and water–phase transitions in cells. *Science* **337,** 1047–1049 (2012).
8. Frey, S., Richter, R. P. & Görlich, D. FG-rich repeats of nuclear pore proteins form a three-dimensional meshwork with hydrogel-like properties. *Science* **314,** 815–817 (2006).
9. Brangwynne, C. P. *et al*. Germline P granules are liquid droplets that localize by controlled dissolution/condensation. *Science* **324,** 1729–1732 (2009).
10. Aggarwal, S. *et al*. Myelin membrane assembly is driven by a phase transition of myelin basic proteins into a cohesive protein meshwork. *PLoS Biol.* **11,** e1001577 (2013).
11. Sackmann, E. How actin/myosin crosstalks guide the adhesion, locomotion and polarization of cells. *Biochim. Biophys. Acta* **1853,** 3132–3142 (2015).
12. Deek, J., Chung, P. J., Kayser, J., Bausch, A. R. & Safinya, C. R. Neurofilament sidearms modulate parallel and crossed-filament orientations inducing nematic to isotropic and re-entrant birefringent hydrogels. *Nat. Commun.* **4,** 2224 (2013).
13. Brangwynne, C. P., Mitchison, T. J. & Hyman, A. A. Active liquid-like behavior of nucleoli determines their size and shape in *Xenopus laevis* oocytes. *Proc. Natl Acad. Sci. USA* **108,** 4334–4339 (2011).
14. Han, T. W. *et al*. Cell-free formation of RNA granules: bound RNAs identify features and components of cellular assemblies. *Cell* **149,** 768–779 (2012).
15. Patel, A. *et al*. A liquid-to-solid phase transition of the ALS protein FUS accelerated by disease mutation. *Cell* **162,** 1066–1077 (2015).
16. Molliex, A. *et al*. Phase separation by low complexity domains promotes stress granule assembly and drives pathological fibrillization. *Cell* **163,** 123–133 (2015).

17. Lin, Y., Protter, D. S. W., Rosen, M. K. & Parker, R. Formation and maturation of phase-separated liquid droplets by RNA-binding proteins. *Mol. Cell* **60,** 208–219 (2015).
18. Xiang, S. *et al*. The LC domain of hnRNPA2 adopts similar conformations in hydrogel polymers, liquid-like droplets, and nuclei. *Cell* **163,** 829–839 (2015).
19. Murakami, T. *et al*. ALS/FTD mutation-induced phase transition of FUS liquid droplets and reversible hydrogels into irreversible hydrogels impairs RNP granule function. *Neuron* **88,** 678–690 (2015).
20. Zhang, H. *et al*. RNA controls PolyQ protein phase transitions. *Mol. Cell* **60,** 220–230 (2015).
21. Kwon, I. *et al*. Poly-dipeptides encoded by the C9orf72 repeats bind nucleoli, impede RNA biogenesis, and kill cells. *Science* **345,** 1139–1145 (2014).
22. Li, Y. R., King, O. D., Shorter, J. & Gitler, A. D. Stress granules as crucibles of ALS pathogenesis. *J. Cell Biol.* **201,** 361–372 (2013).
23. Wippich, F. *et al*. Dual specificity kinase DYRK3 couples stress granule condensation/dissolution to mTORC1 signaling. *Cell* **152,** 791–805 (2013).
24. Khademhosseini, A. & Langer, R. Microengineered hydrogels for tissue engineering. *Biomaterials* **28,** 5087–5092 (2007).
25. Hoare, T. R. & Kohane, D. S. Hydrogels in drug delivery: progress and challenges. *Polymer* **49,** 1993–2007 (2008).
26. Iwasaki, T. & Wang, Y.-L. Cytoplasmic force gradient in migrating adhesive cells. *Biophys. J.* **94,** L35–L37 (2008).
27. Yang, Z. M., Xu, K. M., Guo, Z. F., Guo, Z. H. & Xu, B. Intracellular enzymatic formation of nanofibers results in hydrogelation and regulated cell death. *Adv. Mater.* **19,** 3152–3156 (2007).
28. Hülsmann, B. B., Labokha, A. A. & Görlich, D. The permeability of reconstituted nuclear pores provides direct evidence for the selective phase model. *Cell* **150,** 738–751 (2012).
29. DeRose, R., Miyamoto, T. & Inoue, T. Manipulating signaling at will: chemically-inducible dimerization (CID) techniques resolve problems in cell biology. *Pflüg. Arch. Eur. J. Physiol.* **465,** 409–417 (2013).
30. Tanaka, F. *Polymer Physics: Applications to Molecular Association and Thermoreversible Gelation* (Cambridge Univ. Press, 2011).
31. Li, P. *et al*. Phase transitions in the assembly of multivalent signalling proteins. *Nature* **483,** 336–340 (2012).
32. Lin, Y.-C. *et al*. Rapidly reversible manipulation of molecular activity with dual chemical dimerizers. *Angew. Chem. Int. Ed Engl.* **52,** 6450–6454 (2013).
33. Lin, Y.-C. *et al*. Chemically inducible diffusion trap at cilia reveals molecular sieve-like barrier. *Nat. Chem. Biol.* **9,** 437–443 (2013).
34. McLauchlan, H. J., James, J., Lucocq, J. M. & Ponnambalam, S. Characterization and regulation of constitutive transport intermediates involved in trafficking from the trans-Golgi network. *Cell Biol. Int.* **25,** 705–713 (2001).
35. Kedersha, N., Ivanov, P. & Anderson, P. Stress granules and cell signaling: more than just a passing phase? *Trends Biochem. Sci.* **38,** 494–506 (2013).
36. Souquere, S. *et al*. Unravelling the ultrastructure of stress granules and associated P-bodies in human cells. *J. Cell Sci.* **122,** 3619–3626 (2009).
37. Gilks, N. *et al*. Stress granule assembly is mediated by prion-like aggregation of TIA-1. *Mol. Biol. Cell* **15,** 5383–5398 (2004).
38. Kedersha, N. L., Gupta, M., Li, W., Miller, I. & Anderson, P. RNA-binding proteins TIA-1 and TIAR link the phosphorylation of eIF-2 α to the assembly of mammalian stress granules. *J. Cell Biol.* **147,** 1431–1442 (1999).
39. Kedersha, N. & Anderson, P. Mammalian stress granules and processing bodies. *Methods Enzymol.* **431,** 61–81 (2007).
40. Kimball, S. R., Horetsky, R. L., Ron, D., Jefferson, L. S. & Harding, H. P. Mammalian stress granules represent sites of accumulation of stalled translation initiation complexes. *Am. J. Physiol. Cell Physiol.* **284,** C273–C284 (2003).
41. Guntas, G. *et al*. Engineering an improved light-induced dimer (iLID) for controlling the localization and activity of signaling proteins. *Proc. Natl Acad. Sci. USA* **112,** 112–117 (2015).
42. Taslimi, A. *et al*. An optimized optogenetic clustering tool for probing protein interaction and function. *Nat. Commun.* **5,** 4925 (2014).
43. Lee, S. *et al*. Reversible protein inactivation by optogenetic trapping in cells. *Nat. Methods* **11,** 633–636 (2014).
44. Miyazaki, Y. *et al*. A method to rapidly create protein aggregates in living cells. *Nat. Commun.* **7,** 11689 (2016).
45. Inobe, T. & Nukina, N. Rapamycin-induced oligomer formation system of FRB-FKBP fusion proteins. *J. Biosci. Bioeng.* **122,** 40–46 (2016).
46. Shin, Y. *et al*. Spatiotemporal control of intracellular phase transitions using light-activated optoDroplets. *Cell* **168,** 159–171 (2017).
47. Jucker, M. & Walker, L. C. Self-propagation of pathogenic protein aggregates in neurodegenerative diseases. *Nature* **501,** 45–51 (2013).


## Acknowledgements

We are grateful to N. Kedersha and P. Anderson who provided helpful discussions and reagents related to stress granules, to J. L. Pfaltz who collaborated with A.S.A. to develop a modified C++ code for identifying chordless cycles in graphs, and to R. Reed, A. Ewald, H. Sesaki, M. Iijima and S. Regot for sharing their resources for our experiments. We also extend our appreciation to J. P. Gong, I. Hamachi, R. Yoshida for valuable comments on our work. This work was mainly supported by the Johns Hopkins University Catalyst Fund to T.I., and in part by the National Institutes of Health (NIH) (GM092930, DK102910, CA103175 and DK089502 to T.I., and T32GM007445 to A.S.), and the National Science Foundation (NSF) (CCF-1217213 to J.G.).

## Author contributions

H.N., A.A.L. and T.I. conceived the project. H.N., A.A.L., A.S., Y.-C.L., M.T., R.D. and D.B., performed molecular biology as well as cell biology experiments. H.N., A.A.L., S.R. and A.S. purified proteins under the guidance of W.H. and S.B.G. The biochemical and biophysical experiments were mostly performed by H.N. and A.A.L., and partially by S.R. and Y.-C.L. H.N., A.A.L. and T.I. wrote the manuscript with the help of J.G. A.S.A. and J.G. developed the computational model, analysed the computational results, and wrote the computational parts of the paper. A.S.A. wrote appropriate code and conducted the computational experiments. S.W. performed correlated EM measurement and analysis. E.R. and B.H. performed development and demonstration of light-inducible iPOLYMER with H.N.

## Additional information

Supplementary information is available in the online version of the paper. Reprints and permissions information is available online at www.nature.com/reprints. Publisher's note: Springer Nature remains neutral with regard to jurisdictional claims in published maps and institutional affiliations. Correspondence and requests for materials should be addressed to A.S.A. or T.I.

## Competing financial interests

The authors declare no competing financial interests.

## Methods

**Reagents.** Rapamycin was purchased from LCLab and prepared as dimethylsulfoxide (DMSO) stock solutions. Fluorescently labelled ethylenediamine-core generation-4 hydroxyl-terminated poly(amidoamine) dendrimer, D-Cy5 (ref. 48), was kindly provided by Rangaramurajan M. Kannan's group. CdSeS/ZnS alloyed quantum dots with a 665 nm emission wavelength were purchased from Sigma-Aldrich. FluoSpheres Fluorescent Microspheres (fluorescent polystyrene beads) were purchased from Molecular Probes. Antibodies against G3BP, eIF3b, eIF4G, and ribosomal P antigen, and sodium arsenite were kind gifts from N. Kedersha (Harvard Medical School, USA).

**Computational modelling.** *In silico* implementation of iPOLYMER was based on a realistic kinetic Monte Carlo simulation algorithm, which produced sufficiently accurate approximations of stochastic reaction–diffusion dynamics. Model details and computational analysis can be found in Supplementary Information 1.

The model employs a stochastic biochemical reaction system, which contains three types of molecules, FKBP, FRB and rapamycin. These molecules interact according to four reversible reactions (Fig. 1c) and are subject to random diffusion. The binding sites in FKBP and FRB were labelled as free or bound at each time point, along with the information of binding partners. At a given time, the system may contain a mixture of FKBP, FRB, and rapamycin molecules, as well as aggregate molecules formed by the mutual binding of these three basic molecules. The association/dissociation rates were determined from previous experimental findings[49].

To model iPOLYMER, we spatially discretized the well-known continuous-space Doi model of stochastic reaction–diffusion[50,51], and obtained a physically valid approximation based on the reaction–diffusion master equation (RDME)[52–56]. This led to a Markov process model that describes the time evolution of the location of each basic or aggregate molecule at a resolution of one voxel in the system. We simulated the resulting process by a stochastic kinetic Monte Carlo algorithm. In our computational analysis, we modelled the CID system in a predefined volume of a subcellular size, discretized the system in each spatial direction, resulting in a given number of equally sized voxels that satisfy the modelling assumptions and constraints, and used experimentally verified kinetic rate values for certain reactions as well as plausible values for the kinetic rates of the remaining reactions (see Supplementary Information 1).

**DNA constructs.** Construction of $YF_{xN}$ and $CR_{xM}$: To generate the YFP–FKBP ($YF_{x1}$) and CFP–FRB ($CR_{x1}$) constructs, two distinct polymerase chain reaction (PCR) products encoding FKBP and FRB were digested with BsrGI and XhoI, and inserted into the pEYFP(C1) and pECFP(C1) constructs (Clontech), respectively. To prepare the $YF_{x2}$ and $CR_{x2}$ constructs, FKBP and FRB fragments with a 12-amino-acid linker sequence (SAGGx3) were generated by PCR and cloned into $YF_{x1}$ and $CR_{x1}$ constructs, respectively. The same strategy was used to generate two series of multivalent FKBP and FRB constructs.

Construction of cytoYF$_{xN}$ and cytoCR$_{xM}$: Nuclear export signal from MAPKK was inserted into the NheI and AgeI cloning sites of $YF_{xN}$ and $CR_{xM}$, respectively.

Construction of $YF_{x5}$-His and $CR_{x5}$-His for purification: Coding sequences of $YF_{x5}$ and $CR_{x5}$ were amplified by PCR from the plasmids described above, respectively. The obtained fragments were then digested with NcoI and NotI cloned into the corresponding sites in pET28a.

Construction of RRM-$CR_{x5}$ and RRM-$CR_{x5}$ (pMT2): The YFP-TIA-1 and pMT2 vectors were kindly provided by Paul Anderson's group. The RRM domain was amplified from YFP-TIA-1 using 5′-TAGCTAGCGCCACCATGGAGGACGA GATGCCC-3′ and 5′-ATACCGGT-CCTAGTTGTTCTGTTAGCCCAGAAG-3′. The PCR products were digested with NheI and AgeI, and cloned into the corresponding sites in $CR_{x5}$ to obtain RRM-$CR_{x5}$. RRM-$CR_{x5}$ was then amplified by 5′-ACGCCTGCAGGGCCACCATGGAGGACGAG-3′ and 5′-ACGCAATTGTCA GTTATCTAGATC-CGGTGG-3′, and digested by SbfI and MfeI. The digested fragments were then cloned into the PstI and EcoRI cloning sites of the pMT2 vector to obtain TIA-1RRM-$CR_{x5}$ (pMT2). Overexpression of many stress granule-associated proteins induces spontaneous stress granules in the absence of additional stress. It is known that pMT2 vector may express inhibitors of the eIF2α kinase PKR, which is required for the spontaneous stress granule formation[39]. We therefore adopted the pMT2 vector to inhibit excessive formation of stress granules in some experiments.

Construction of mCherry-iLID$_{x6}$, YFP-SspB$_{x6}$, RRM-mCherry-iLID$_{x6}$ and RRM-YFP-SspB$_{x6}$: We synthesized DNA sequence encoding three tandem iLID and SspB (Genscript), and subcloned two tandem sequences of them in pmCherry(C1) and pEYFP(C1) vectors, respectively, between BglII and BamHI sites in the original vectors, taking advantage of the compatible ends cleaved by the two restriction enzymes. To construct RRM domain-functionalized constructs, DNA fragments encoding TIA-1 RRM domains were cut out of RRM-$CR_{x5}$ by NheI and AgeI, and subcloned into mCherry-iLID$_{x6}$ or YFP-SspB$_{x6}$.

**Cell culture and transfection.** COS-7 cells (purchased from ATCC) were cultured in a DMEM (GIBCO) medium supplemented with 10% fetal bovine serum (FBS) and 1% Penicillin Streptomycin (Life Technologies) in a 37 °C and 5% $CO_2$ incubator. Cells were checked for mycoplasma contamination by PCR. Cells were transiently transfected using either FugeneHD (Roche) or Amaxa Nucleofector (Lonza) and seeded in 8-well chamber slides (Thermo).

**Cellular imaging of iPOLYMER puncta formation.** Cells were transfected with desired constructs, seeded in 8-well chamber slides and incubated for 36–48 h. The culture medium was then washed and replaced with Dulbecco's Phosphate-Buffered Saline (DPBS, Gibco) for imaging. Imaging was conducted with an Olympus inverted microscope and a Zeiss LSM 780 confocal imaging system. FRAP experiments were conducted on Zeiss LSM 780. All images were processed using Metamorph imaging software (Molecular Devices). For inducing hydrogel formation by iPOLYMER, rapamycin in DMSO was diluted with DPBS to 3.33 μM and added to the chamber in a 1:10 dilution.

**Quantification of iPOLYMER puncta formation.** COS-7 cells were simultaneously transfected with cytoYF$_{xN}$ and cytoCR$_{xM}$ and grown 36–48 h as described above. Rapamycin was then added (333 nM) and cells incubated 20 min at 37 °C with 5% $CO_2$. Cells were then fixed with 4% (w/v) paraformaldehyde and imaged on a Zeiss Axiovert 135 TV microscope with a QIclick camera (QImaging). For each cell imaged, a $Z$-stack of five planes separated by 1 μm was taken to ensure that any puncta present in the cell would be observed. Cells were considered to be punctated if at least one punctum with both YFP and CFP fluorescence was present, and to be non-punctuated if no such structure was present. The mean ± s.e.m. from three independent experiments was then measured.

**FRAP experiment and analysis.** All FRAP experiments were carried out with a Zeiss LSM780 confocal microscope using bleaching. In the FRAP evaluation of the turnover rates of the iPOLYMER peptides, data was acquired by raster scanning. YFP was photobleached by a 514 nm laser within a circular ROI for bleaching. The fluorescence intensity within the ROI was monitored, and was normalized to the intensity before bleaching. The normalized fluorescence recovery over time, $F(t)$, was then fitted to an exponential function;

$$F(t) = F_\infty - A\exp\left(-\frac{t}{\tau_{1/2}\ln 2}\right) \quad (1)$$

to obtain the mobile fraction $F_\infty$, half-recovery time $\tau_{1/2}$, and $A$ as fitted parameter values.

To monitor the diffusion of the tracers mCherry or mCherry-β-galactosidase within the iPOLYMER puncta, higher resolution was required in terms of both space and time. We therefore adopted line-scan data acquisition for a higher frame rate, and a spot-bleach method at a single spot without scanning for photobleaching. To achieve sufficiently high spatio-temporal resolution, the FRAP experiment was carried out with micrometre-sized puncta 24 h after rapamycin administration. Fluorescence recovery at the bleaching spot was monitored and analysed by fitting the normalized fluorescence intensity transient $F(t)$ to the following function:

$$F(t) = F_\infty - A_s\exp\left(-\frac{t}{\tau_s}\right) - A_f\exp\left(-\frac{t}{\tau_f}\right), \quad (\tau_s > \tau_f) \quad (2)$$

to obtain five fitting parameter values, $F_\infty, A_s, A_f, \tau_s$, and $\tau_f$, where $F_\infty$ is the immobile fraction, $A_s$ and $A_f$ are the amplitudes of the slower and faster recovery components, respectively, and $\tau_s$ and $\tau_f$ are characteristic decay times for the slower and faster components, respectively. To characterize the diffusion kinetics by a single parameter, we computationally quantified the half-recovery time $\tau_{1/2}$ by interpolation (Supplementary Fig. 5.4c). Briefly, the fitted function was plotted with time step $\Delta t = 0.1$ ms. The time required for half-recovery was then calculated by linear interpolation between the plotted data points to obtain $\tau_{1/2}$. All fittings were done with Igor Pro software (WaveMetrics), using built-in curve fitting formulae and functions.

**Protein purification and *in vitro* hydrogel formation.** $YF_{x5}$-HisC and $R_{x5}$-His vectors were used to transform the BL21(DE3) *Escherichia coli* host strain (Novagen). Protein expression was induced by 0.1 mM isopropyl β-D-1-thiogalactopyranoside and the proteins in the supernatant were bound to Ni-nitrilotriacetate resin (Qiagen). After elution by 250 mM imidazole, the eluted fraction was dialysed and purified further by Mono Q 5/50 GL anion exchange column. Purified $YF_{x5}$ and $CR_{x5}$ were premixed in 20 mM Tris pH8.5, 300 mM NaCl. Subsequently, rapamycin stock in DMSO was added with a 1:100 dilution and immediately mixed vigorously. For the experiments associated with pore-size estimation, the solution was further centrifuged at 16,000$g$ for 30–60 min at room temperature. Pellets were suspended again in the solution by brief pipetting, transferred onto the coverslip, and the solution containing both fluorescent tracer and rapamycin was added on top. The penetration of the fluorescent tracers was examined using a LSM780 confocal microscope (Zeiss).

**TGN38 vesicle movement analysis.** Cells were transiently transfected with TGN38-mCherry, cytoYF$_{x5}$ and cytoCR$_{x5}$. Cells were first induced to form iPOLYMER for 1 h, then imaged while maintained at 37 °C and 5% $CO_2$. Images were taken every 5 s. The velocity of the TGN38-positive vesicles was estimated by dividing the distance that the vesicles travelled within the *xy* plane between two consecutive frames by the 5 s interval. The images were analysed using the 'track points' function in the Metamorph image analysis software (Molecular Devices).

**Induction of physiological stress granules and their analogues.** To induce stress granule formation, cells were incubated in 0.5 mM sodium arsenite-containing culture media for 30 min. For stress granule analogues, cells were transfected as described above with RRM-CR$_{x5}$ or RRM-CR$_{x5}$ (pMT2) using cytoYF$_{x5}$. The cells were allowed to grow for 36–48 h before rapamycin administration. The rest of the experiment was carried out as described above.

**Electron microscopy.** For correlative EM, cells were cultured on sapphire disks that are carbon-coated with a grid pattern. This pattern was used to locate the region of interest in an electron microscope. Following poly-D-lysine coating, cells were cultured overnight on the sapphire disks in a 24-well culture plate before the transfection. The iPOLYMER formation was induced 24 h after transfection for 1 h at 333 nM rapamycin, and cells were fixed with 4% paraformaldehyde (in PBS) for 5 min. Cells were subsequently washed with PBS three times and then imaged with a fluorescence microscope in the culture plate. Fluorescence images of iPOLYMER puncta-containing cells were obtained with a 20× objective lens. Bright-field images of the carbon grid pattern on the sapphire disks were simultaneously obtained to locate the cells in later steps.

Following fluorescence imaging, cells were prepared for EM. To avoid shrinkage of cells during the dehydration process, cells were frozen on a high-pressure freezer (Leica EM ICE). The vitrified specimens were handled carefully under liquid nitrogen and placed into cryo-tubes containing 1% osmium tetroxide (EMS #19132), 1% glutaraldehyde (EMS #16530), 1% water, and anhydrous acetone (EMS #10016). The freeze substitution was performed in a Leica AFS2 unit with the following program: 8 h at −90 °C, a ramp at 5 °C h$^{-1}$ to −20 °C, 12 h at −20 °C, and a ramp at 10 °C h$^{-1}$ to 20 °C. The specimens were then embedded into epon-araldite resin and cured for 48 h. The region of interest was located based on a grid pattern. The plastic block was trimmed to the region of interest and sectioned with a diamond knife using an ultramicrotome (Leica UC8). Approximately 40 consecutive sections (40 nm each) were collected onto the pioloform-coated grids and imaged on a Phillips transmission electron microscope (CM120) equipped with a digital camera (AMT XR80). The fluorescence and electron micrographs were roughly aligned based on the carbon-coated grid patterns. The alignment was slightly adjusted based on the visible morphological features. EM images of the stress granules were obtained similarly, but without any correlation.

**Immunostaining.** Cells were fixed with 4% (w/v) paraformaldehyde, permeabilized with 0.2% (v/v) Triton X-100 for 30 min, and blocked by 1% (w/v) BSA in PBS. A monoclonal antibody against PABP-1 (10E10; Sigma-Aldrich), G3BP1 (sc-81940; Santa Cruz), eIF4G (sc-11373; Santa Cruz), and eIF3b (sc-16377; Santa Cruz) were used at a 1:500-800 dilution. The secondary antibodies were Alexa Fluor 594- or 647-labelled anti IgG of the appropriate species (anti-human antibodies were purchased from Jackson Immunoresearch, others from Invitrogen), with a 1:1,000 dilution. For longer administration conditions (24 h), rapamycin was used at 100 nM. After the staining, cells were imaged with a Zeiss Axiovert 135 TV microscope equipped with a QIclick camera (QImaging), or a Nikon eclipse Ti microscope equipped with a Zyla sCMOS camera (Andor). For imaging Alexa Fluor 594 and 647, filter sets for mCherry and Cy5 were used, respectively.

**Light-inducible iPOLYMER-LI puncta formation.** For live-cell imaging, cells were transfected with mCherry-iLID$_{x6}$ and YFP-SSBP$_{x6}$, incubated for 12–24 h, then observed under the LSM780 confocal microscope (Zeiss). Using the bleaching function of the microscope, cells were stimulated by a 488 nm laser before each frame during the stimulus. For imaging, YFP and mCherry signals were excited by 514 nm and 564 nm lasers, respectively.

For the immunostaining study of iPOLYMER-LI puncta, we used for stimulation a custom-made blue light LED illuminator kindly provided from Sergi Regot's group. Cells were transfected with mCherry-iLID$_{x6}$ and YFP-SSBP$_{x6}$ or the constructs functionalized with TIA-1 RRM domains, incubated for 24 h, and stimulated by the illuminator in the incubator for 1 h. Cells were then fixed and immunostained as described above.

**Statistical analysis.** A two-tailed Student's *t*-test was used for all statistical analyses, after confirming that the variance was similar between the groups compared. The sample size was chosen so that the distribution is not deviated from normal distribution and the saturation of the mean value or the proportion was reached. Some *in vitro* experiments may not include theoretically sufficient number of samples due to the limited resource required. The s.e.m. was used to generate error bars in the figures unless the result was too small to be visible on the plot.

**Code availability.** MATLAB software for implementing the RDME-based model as well as an executable version of Pfaltz's chordless cycle finder can be freely downloaded from www.cis.jhu.edu/∼goutsias/CSSlab/software.html. Computational analysis data and queries should be addressed to A.S.A. (aas.afshar@gmail.com).

**Data availability.** Data supporting the findings described in the manuscript are available within the article and its supplementary information files and available from the corresponding author upon reasonable request. DNA plasmids used have been deposited to Addgene with accession codes 103774-103785.

## References


48. Lesniak, W. G. *et al*. Biodistribution of fluorescently labeled PAMAM dendrimers in neonatal rabbits: effect of neuroinflammation. *Mol. Pharm.* **10,** 4560–4571 (2013).
49. Banaszynski, L. A., Liu, C. W. & Wandless, T. J. Characterization of the FKBP.rapamycin.FRB ternary complex. *J. Am. Chem. Soc.* **127,** 4715–4721 (2005).
50. Doi, M. Second quantization representation for classical many-particle system. *J. Phys. Math. Gen.* **9,** 1465–1477 (1976).
51. Doi, M. Stochastic theory of diffusion-controlled reaction. *J. Phys. Math. Gen.* **9,** 1479–1495 (1976).
52. Isaacson, S. A. A convergent reaction–diffusion master equation. *J. Chem. Phys.* **139,** 54101 (2013).
53. Isaacson, S. A. & Peskin, C. S. Incorporating diffusion in complex geometries into stochastic chemical kinetics simulations. *SIAM J. Sci. Comput.* **28,** 47–74 (2006).
54. Isaacson, S. A. Relationship between the reaction–diffusion master equation and particle tracking models. *J. Phys. Math. Theor.* **41,** 65003 (2008).
55. Fange, D., Berg, O. G., Sjöberg, P. & Elf, J. Stochastic reaction–diffusion kinetics in the microscopic limit. *Proc. Natl Acad. Sci. USA* **107,** 19820–19825 (2010).
56. Hellander, S., Hellander, A. & Petzold, L. Reaction–diffusion master equation in the microscopic limit. *Phys. Rev. E Stat. Nonlin. Soft Matter Phys.* **85,** 42901 (2012).